



HAL
open science

Hydrogen generation performances and electrochemical properties of Mg alloys with 14 H long period stacking ordered structure

Manuel Legrée, Véronique Charbonnier, Serge Al Bacha, Kohta Asano, Kouji Sakaki, Isabelle Aubert, Fabrice Mauvy, Jocelyn Sabatier, Jean-Louis Bobet

► To cite this version:

Manuel Legrée, Véronique Charbonnier, Serge Al Bacha, Kohta Asano, Kouji Sakaki, et al.. Hydrogen generation performances and electrochemical properties of Mg alloys with 14 H long period stacking ordered structure. *Journal of Alloys and Compounds*, 2023, 937, pp.168154. 10.1016/j.jallcom.2022.168154 . hal-03932299

HAL Id: hal-03932299

<https://hal.science/hal-03932299>

Submitted on 10 Jan 2023

HAL is a multi-disciplinary open access archive for the deposit and dissemination of scientific research documents, whether they are published or not. The documents may come from teaching and research institutions in France or abroad, or from public or private research centers.

L'archive ouverte pluridisciplinaire **HAL**, est destinée au dépôt et à la diffusion de documents scientifiques de niveau recherche, publiés ou non, émanant des établissements d'enseignement et de recherche français ou étrangers, des laboratoires publics ou privés.

Hydrogen generation performances and electrochemical properties of Mg alloys with 14H Long Period Stacking Ordered structure.

M. Legrée^{a*}, V. Charbonnier^b, S. Al Bacha^c, K. Asano^b, K. Sakaki^b, I. Aubert^d, F. Mauvy^a, J. Sabatier^e, J.-L. Bobet^a.

^a CNRS, Univ. Bordeaux, Bordeaux INP, ICMCB, UMR 5026, F-33600 Pessac, France.

^b National Institute of Advanced Industrial Science and Technology, 16-1 Onogawa, Tsukuba, Ibaraki 305-8569, Japan.

^c Equipe de Recherche et d'Innovation en Electrochimie pour l'énergie (ERIEE), Institut de Chimie Moléculaire et des Matériaux d'Orsay (ICMMO), UMR CNRS 8182, Université Paris-Saclay, 91405 Orsay, France.

^d University of Bordeaux, CNRS, Arts et Métiers Institute of Technology, Bordeaux INP, INRAE, I2M Bordeaux, F-33400 Talence, France.

^e CNRS, Univ. Bordeaux, Bordeaux INP, IMS, UMR 5218, 33405 Talence, France.

Abstract

Hydrolysis of Magnesium with water is an excellent way to produce H₂ at high rate, especially when alloyed with nobler elements that accelerate its corrosion. In this work, the hydrogen generation properties of four Magnesium based alloys with Long Period Stacking Ordered (14H-LPSO) structures (Mg₉₁Cu₄Y₅; Mg₉₁Ni₄Y₅; Mg₉₁Ni₄Gd₅ and Mg₉₁Ni₄Sm₅) are studied through standard electrochemical methods. The hydrolysis experiment on coarse powder are coherent with the electrochemical measurements performed on polished surface. The rare earth (Y, Gd or Sm) and transition metal (Ni or Cu) involved in the LPSO are found to have a significant influence on the corrosion and hydrolysis properties of alloys with 14H-LPSO structures.

Keywords: Magnesium, LPSO, hydrolysis, Corrosion, Electrochemical Impedance Spectroscopy, hydrogen production

* corresponding author: manuel.legrée@icmcb.cnrs.fr (M. Legrée).

1. Introduction

With twelve protons, magnesium (Mg) is one of the lightest metals (1.738 g/cm^3) and among the most available on our planet (7th most abundant element on earth's crust) [1]. In addition, it has good electrical and thermal conductivities, interesting mechanical properties and is biocompatible (Mg^{2+} is the 4th most abundant cation in human body) [2,3]. These characteristics make magnesium a very interesting material for many applications such as lightweight structure materials, transport, electronics, energy, fracturing ball technologies or biodegradable implants [2–7]. Widening Mg alloys usability has motivated extensive scientific research on their oxidation and corrosion properties [6,8–22]. There are several key features that make magnesium and its alloys a peculiar topic in the field of corrosion science. First, magnesium has a very low corrosion potential (-1.7 V/SCE (Saturated Calomel Electrode) in aqueous solutions) and is highly sensitive to corrosion, particularly to galvanic corrosion [23]. It is frequently used as sacrificial anode in the industry. Furthermore, enhanced hydrogen evolution occurs under anodic polarization [8,15,24,25] and a discrepancy is thus observed between corrosion rates measured from electrochemical methods and mass loss and H_2 collection [26]. Due to its strong ability to corrode, Mg has attracted a lot of interest for di-hydrogen (H_2) production via hydrolysis reaction [27–33]

Among Mg alloys, Long Period Stacking Ordered (LPSO) is the name given to a family of structures found in some Mg-Transition Metal (TM)-Rare Earth (RE) systems [34–37]. Because of the presence of TM in the structure, LPSO shows higher corrosion potential than pure Mg which leads to galvanic coupling between the two phases (*i.e.* Mg and LPSO) [38,39]. In the literature, the Mg-Y-Zn system (in which Inoue *et al.* [40] discovered Mg-LPSO structure for the first time) is by far the most studied one [37,40–44]. Mg-Gd-Zn, Mg-Gd-Y-Zn and Mg-Y-Ni systems were studied for biodegradable implants and fracturing ball applications [39,45,46]. In both cases, corrosion resistance is not desired too important because the alloy is required to dissolve after use, this is why researchers focus on controlling the degradation rate of the material. Beyond these few examples, reported works on corrosion of LPSO containing other elements than zinc (Zn) and yttrium (Y) remain very scarce. Additionally, recent study led in our group suggested that LPSO can be very efficient materials for H_2 generation via hydrolysis [47].

It is common practice to lead hydrolysis experiment with Mg powder or end of life alloys scraps with a roughened surface for optimized hydrogen generation performances (*i.e.* activated by ball milling) [29,48,49]. In such conditions, the reacting surface is not well defined and it evolves importantly throughout the reaction. The present work aims at comparing the behavior of Mg-LPSO alloys under hydrolysis conditions (*i.e.* as gross powders) with electrochemical measurements led on

bulk surfaces. To achieve this goal, four samples were prepared by induction melting of pure elements and annealing, namely: $Mg_{91}Cu_4Y_5$, $Mg_{91}Ni_4Y_5$, $Mg_{91}Ni_4Gd_5$ and $Mg_{91}Ni_4Sm_5$. Samples were characterized physically and chemically with X-Ray Diffraction (XRD), Scanning Electrochemical Microscopy (SEM) and Energy Dispersive X-ray Spectroscopy (EDXS). Hydrolysis reactions with powders are presented and further interpreted in the light of standard electrochemical characterization on bulk materials surfaces. The techniques involved are chronopotentiometry (Open Circuit Potential (OCP) recording versus time), Electrochemical Impedance Spectroscopy (EIS) and potentiodynamic polarization (data is analyzed using Tafel method).

2. Materials and methods

The compounds involved in the present study were synthesized using chunks of magnesium (99.9%) from Kojundo Chemical Laboratory Co., Ltd., copper (Cu) (99.99%) and nickel (Ni) (99.9%) from Furuuchi Chemical Co., and all Rare Earths (RE) (Yttrium (Y), Gadolinium (Gd) and Samarium (Sm)), 99.9% from Nippon Yttrium Co., Ltd. The pure elements were melted together in an induction furnace under helium atmosphere. Due to its high vapor pressure, an excess of 7 wt.% of Mg was systematically added. The obtained ingots were subsequently annealed for 10 days under argon atmosphere at 500°C in a tantalum foil.

Synthesized alloys were characterized by XRD using a Philips PANalytical X'Pert (PW1820) diffractometer with Cu $K\alpha_1$ radiation ($\lambda=1.5405 \text{ \AA}$). SEM observations were made using a TESCAN VEGA3 SB and SERON TECHNOLOGY microscope equipped with Secondary Electron and Back Scattered Electron detectors (hereafter referred to as SE and BSE modes respectively). Furthermore, the elemental composition of the surface was estimated using EDX spectrometer.

All electrochemical measurements were performed in simulated seawater solution (*i.e.* 0.6 mol/L NaCl) at room temperature with a three electrodes set-up (Working Electrode: bulk samples were abraded up to 4000 grit SiC with ethanol as lubricant prior to each electrochemical test; Counter Electrode: Titanium net; Reference Electrode: Saturated Calomel Electrode (SCE) - Hg/Hg_2Cl_2). EIS and polarization measurements were made after 40 min OCP stabilization (except in the case where immersion time is varied as a parameter). OCP and potentiodynamic polarization measurements were done with VersaSTAT 4 potentiostat and controlled via VersaStudio software. Anodic and cathodic polarization curves were recorded separately with a scan rate of 0.5 mV/s as follows: (i) a first sweep from +50 mV to -250 mV vs OCP for the cathodic polarization measurement and (ii) from -50 mV to +250 mV vs OCP for the anodic polarization measurement. EIS diagrams were recorded from 100 kHz to 50 mHz with 10 mV amplitude versus OCP on a Biologic SP-150 potentiostat because of its good stability in AC mode. The data was collected on EC-Lab software and fitted using the commercial Zview

software while Kramers-Kronig relations and Distribution of Relaxation Times (DRT) calculations were done with in-house CANELEIS software using Tikhonov regularization method with weighing parameter $\lambda=10^{-2}$ [50]. In order to help emphasize electrochemical features from these measurements, different immersion times prior to measurements and different rotation speeds of the working electrode were tested. Rotating Disc Electrode (RDE) measurements were carried out with an Origatrod electrode connected to an Origaflex potentiostat.

The reaction of magnesium with water (hydrolysis process) considered in this study is:



Kinetic study of hydrolysis reactions was carried out in a closed 100 mL three-neck round bottom flask connected to a burette that dips in a beaker of water. The experimental setup was previously described in ref [51]. Water from the beaker is initially sucked up into the burette. Then, the di-hydrogen (H_2) produced during the experiment induces water displacement back to the beaker and a balance connected to a computer records the mass variation, allowing to follow in real time the hydrogen generation. Bulk samples were filed and about 30 mg of material were taken to react with 20 mL of simulated seawater solution (*i.e.* 0.6 mol/L NaCl). The solution was rapidly stirred with a magnetic bar and during the whole experiment, the temperature was kept at a constant value of 25°C. After measurement, 1 mL of 2.4 mol/L HCl was added to complete the hydrolysis process and thereby generate the maximum H_2 amount the sample could release. The yield of reaction was calculated from this amount of H_2 .

3. Results and discussion

3.1. Material characterization

Four LPSO compounds have been selected and characterized by X-ray diffraction (XRD): $\text{Mg}_{91}\text{Cu}_4\text{Y}_5$; $\text{Mg}_{91}\text{Ni}_4\text{Y}_5$; $\text{Mg}_{91}\text{Ni}_4\text{Gd}_5$; $\text{Mg}_{91}\text{Ni}_4\text{Sm}_5$. The associated patterns are reported on figure 1 and show that the four alloys synthesized formed LPSO with a 14H structure. LPSO structures can be described as alternating layers of Mg and Mg-TM-RE layers containing L_{12} -type atomic clusters (TM_6RE_8). In the case of 14H studied here, Mg layers are four atomic planes wide. The “H” stands for “Hexagonal” and the “14” gives the number of atomic planes in a unit cell (counted along c direction). Detailed information on LPSO structures can be found in dedicated works [35,52–56].

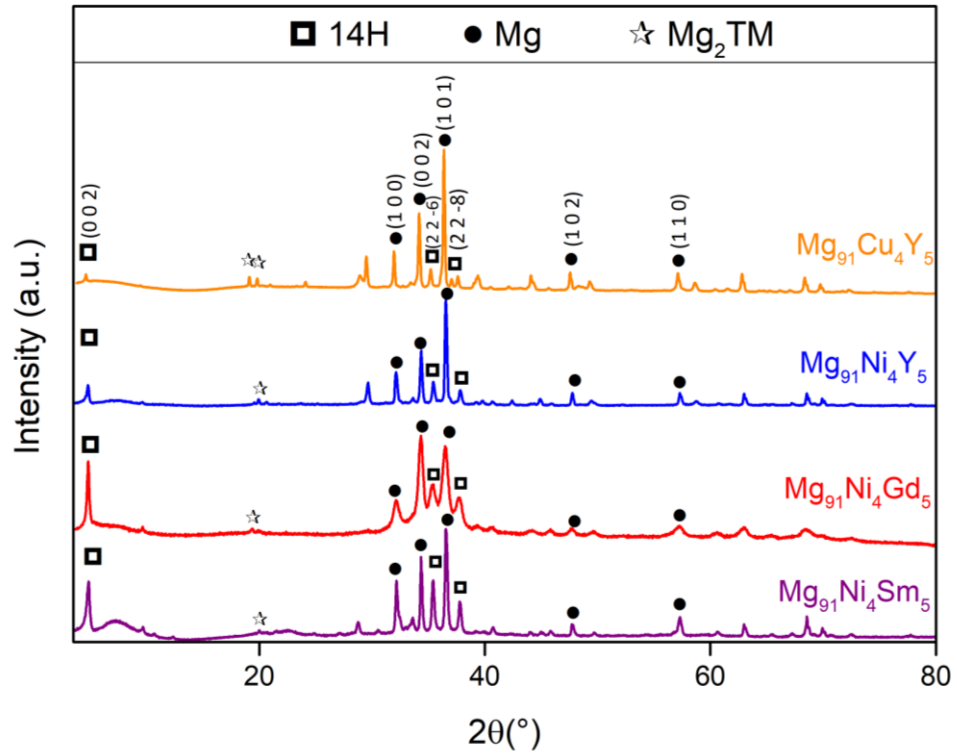


Figure 1 : X-ray diffraction patterns on powders filed from bulk alloys.

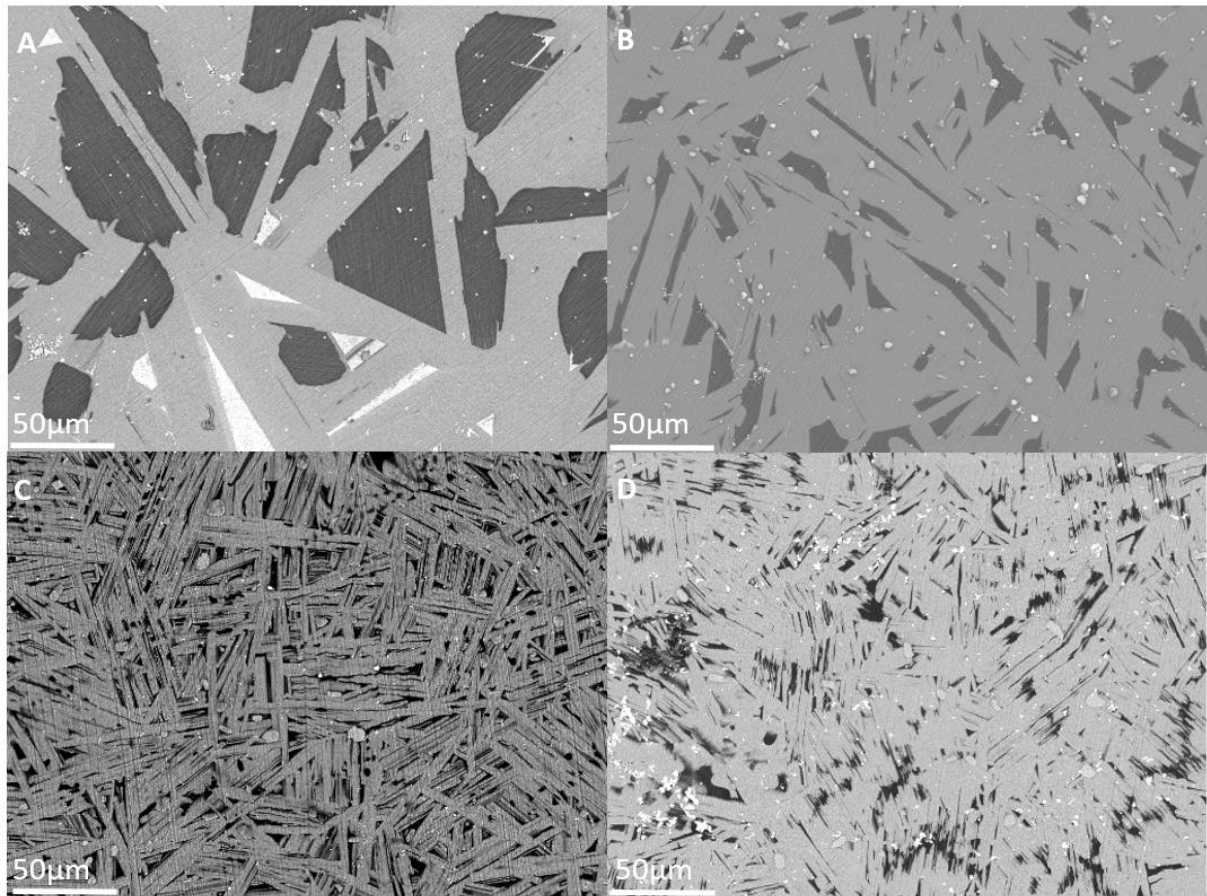


Figure 2: BSE-SEM micrographs of : A- Mg₉₁Cu₄Y₅, B- Mg₉₁Ni₄Y₅, C- Mg₉₁Ni₄Gd₅ and D- Mg₉₁Ni₄Sm₅. The clear zones (majoritarian) are LPSO phases, the dark zones are Mg phase and the small bright areas are Mg₂TM or Y₂O₃.

The microstructures of the elaborated samples have been characterized using SEM micrographs and EDXS analysis. Main and secondary phases identification, surface proportions and deduced experimental compositions are summarized in Table 1. The discrepancy observed between measured and theoretical LPSO compositions has already been reported and may be explained by Mg insertion or substitution in the TM_6RE_8 cluster [47,55,57]. It can be deduced from BSE-SEM images of figure 2 that all studied alloys present both LPSO (bright zones) and Mg (dark zones) phases with Mg surface proportions ranging from 15% to 27%. These values were estimated using contrast thresholding with Image J software (with an accuracy of about 2%). In addition, Figure 2 shows that the size and the morphology of Mg inclusions are quite large and well defined in alloys containing Y as RE, while alloys with Sm and Gd present a very intricate Mg phase. According to the EDXS analysis, the white particles visible on the BSE-SEM micrographs correspond to RE_2O_3 and Mg_2TM . The surface proportion for these secondary phases has been estimated to be inferior to 4% by image analysis (Table 1). EDXS measurements revealed variations in the LPSO composition of each alloy. It results in very different TM/RE ratios in the 14H-LPSO phases with different elements, that range from 0.6 for $Mg_{91}Ni_4Y_5$ to 1.1 for $Mg_{91}Ni_4Sm_5$ (the 14H LPSO theoretical value being 0.75). It should be noted here that EDXS allows only for semi-quantitative characterization. The values discussed here are thus used to compare the different alloys but should not be taken as exact composition values.

Table 1 : Studied alloys and their corresponding characterization features.

Alloy	Main Phases (XRD,EDXS)	Secondary phases (XRD,EDXS)	Mg surface proportion (BSE, % Image J)	Secondary phases surface proportion (BSE, % Image J)	EDXS measurement on LPSO	
					Composition	TM/RE atomic ratio
$Mg_{91}Cu_4Y_5$	14H+Mg	Mg_2Cu , Y_2O_3	27	3.6	$Mg_{90}Cu_{4.5}Y_{5.5}$	0.82
$Mg_{91}Ni_4Y_5$	14H+Mg	Mg_2Ni , Y_2O_3	15	1.8	$Mg_{92}Ni_3Y_5$	0.60
$Mg_{91}Ni_4Gd_5$	14H+Mg	Mg_2Ni	21	< 1	$Mg_{91.2}Ni_{3.9}Gd_{4.9}$	0.80
$Mg_{91}Ni_4Sm_5$	14H+Mg	Mg_2Ni , Sm_2O_3	16	2.9	$Mg_{91.4}Ni_{4.5}Sm_{4.1}$	1.10

3.2. Di-hydrogen generation

All four alloys were filed into coarse powders to generate di-hydrogen gas (H_2) by water hydrolysis. The associated kinetic curves are displayed in figure 3 along with the performances of pure Mg and Mg-Ni-C powder. Mg-Ni-C mixture is considered as reference material whose preparation has been optimized in previous works [29,58,59]. It consists in a ball milling of 3 hours at 250 rpm of 95%wt. Mg powder (99.98%), 5%wt. Ni powder (99.98%) and 5%wt. graphite. Even without prior surface activation, $Mg_{91}Ni_4Sm_5$ and $Mg_{91}Ni_4Gd_5$ gross powders present hydrogen generation performances (*i.e.* kinetics and yields) comparable with an optimized mixture. Hydrolysis experiment confirms the strong potential of LPSO materials as efficient hydrogen production materials. $Mg_{91}Cu_4Y_5$ has a much lower H_2 generation kinetic compared to alloys containing Ni as TM. For this alloy, two stages with different gas generation speeds can be distinguished on figure 3. The transition between the two kinetic stages that occurs when about 30%at. of the alloy is consumed could be linked to the prior reaction of Mg phase (which would be consistent with SEM estimation). The alloys with Ni as TM also present different kinetics depending on the RE involved.

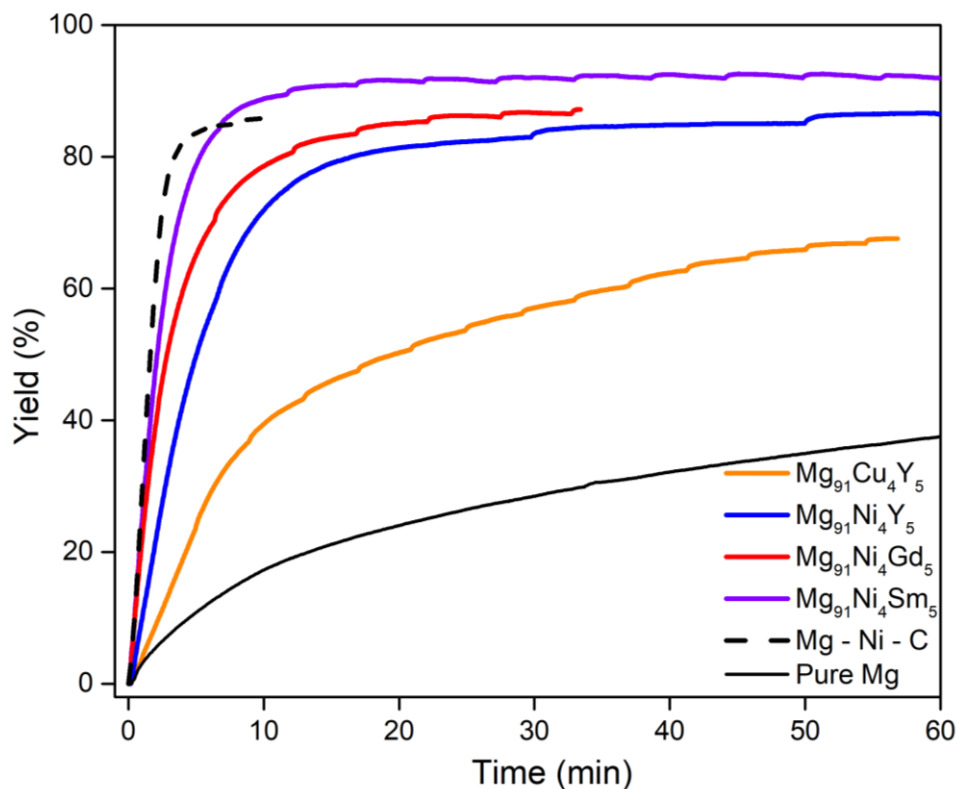


Figure 3 : Hydrolysis at 25°C in 0.6 mol/L NaCl solution with approximately 5% accuracy.

The hydrolysis reactions of the different alloys showed very different features depending on the TM and RE involved in the LPSO phase. Hydrogen generation properties of the alloys will be further investigated in the next sections with electrochemical characterization of bulk material's surface.

3.3. Electrochemical measurements

3.2.1. Open Circuit Potential

Open Circuit Potentials (OCP) were recorded versus time in 0.6 mol/L NaCl solution and are presented in figure 4. OCP of pure Mg is also reported as a matter of comparison. It is interesting to note that $Mg_{91}Ni_4Y_5$, $Mg_{91}Ni_4Gd_5$ and $Mg_{91}Ni_4Sm_5$ alloys have almost identical stabilized OCP values (close to -1.35V/ECS). The nature of the RE involved in the LPSO phase does not seem to influence much the steady state potential of the alloy. This result can be analyzed considering that, in NaCl solutions, RE elements have relatively close corrosion potentials neighboring that of magnesium [60,61].

OCP recording versus time shows that thermodynamic equilibrium of Cu containing alloy is closer to that of pure Mg as compared to Ni containing alloys (figure 4). Mg in $Mg_{91}Cu_4Y_5$ may thus be less likely to corrode than in $Mg_{91}Ni_4RE_5$ alloys with nobler nature. This statement is consistent with hydrolysis experiments in which reaction kinetic was clearly lower for $Mg_{91}Cu_4Y_5$. The hydrolysis kinetics of the three $Mg_{91}Ni_4RE_5$ alloys were slightly different and their stabilized OCP about even. It can be deduced here that the transition metal strongly influences the OCP voltage in the $Mg_{91}TM_4RE_5$ alloys while the RE does not. Hydrolysis experiments for $Mg_{91}Ni_4RE_5$ alloys may thus be understood from kinetics perspective explored in the next sections.

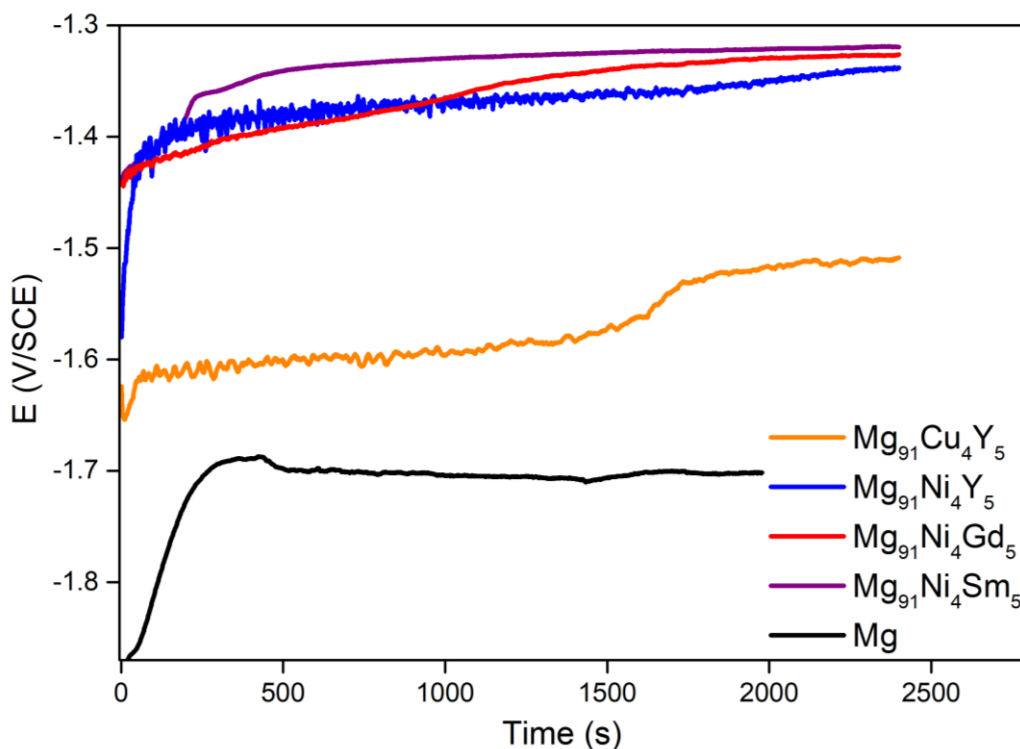


Figure 4 : Open Circuit Potentials (OCP) versus time at 25°C in 0.6 mol/L NaCl solution with approximately 1% accuracy.

After 2400s of immersion, the surfaces of the samples are in major part covered of black corrosion product. This phenomenon have been assigned to magnesium hydroxide precipitation : $MgOH_2$ formation has been confirmed by XRD in previous work [47]. Electrochemical measurements (EIS and polarization) have been performed when the OCP are stabilized, *i.e.* after 2400s of immersion.

3.2.2. Electrochemical Impedance Spectroscopy

The EIS diagrams were recorded between 0.1 Hz and 100 000 Hz with 10 mV of amplitude. In order to verify the stationarity of the system, Kramers-Kronig relations were used [50,62]. As shown in figures 5A and 5B, the results have good correlation both for real and imaginary parts, which indicates that the data is consistent and causal in the range 1Hz – 100 000Hz. According to the literature, in the low frequency range (*i.e.* $\text{freq} \rightarrow 0$ Hz), the real part of the impedance can be assigned to the electrode polarization resistance, which is inversely proportional to the corrosion rate of the alloy ($J_{\text{corr}}=B/R_p$) [21]. In the present study, alloys with LPSO phase are corroding so rapidly that a steady state (*e.g.* stable OCP, same surface condition ...) cannot be held for the long time required by low frequencies measurements. Thus, J_{corr} could not be determined by EIS. The Nyquist diagram of Mg of figure 6A and the corresponding Bode plot of figure 6B both show two well-separated relaxation frequencies, in the high frequency (HF) range and in the medium frequency range (MF). In contrast to pure Mg, LPSO bode plots (figure 6B) are flattened at HF. The DRT calculation method allowed to evidence the relaxation times from EIS data [50,63]. The DRT spectra of figure 7 confirm the presence of two relaxation times in the case of Mg (at *ca.* 40 Hz and 1000 Hz) while for LPSO a multiplicity of peaks with lower intensity appears (illustrated with $Mg_{91}Ni_4Y_5$ on figure 7). As LPSO containing alloys corrode more than pure Mg, their impedance magnitude is smaller (figure 6A compares pure Mg and $Mg_{91}Cu_4Y_5$ Nyquist plots) and different time constants may appear because of the irregularity of the surface, roughened by corrosion. Surface irregularities lead to impedance distribution and result in a strong convolution of the HF and MF peaks that cannot be distinguished in the case of alloys with LPSO (figure 5B). The multiple DRT peaks of LPSO should not be attributed to different mechanisms but to spreading of relaxation time due to irregular surface. The EIS data of alloys with LPSO is thus fitted with the same model as pure Mg, with only two contributions (HF and MF). Constant Phase Elements (CPE) have been used to account for the distributed impedance responses by introduction of α exponent ($0 < \alpha < 1$). Capacity values discussed below are effective capacities calculated as follows:

$$C_{eff} = \frac{(R*Q)^{1/\alpha}}{R} \quad (2)$$

with C_{eff} the effective capacity, R the corresponding resistance parallel to the CPE, Q the CPE capacity and α the exponent that reflects the impedance distribution.

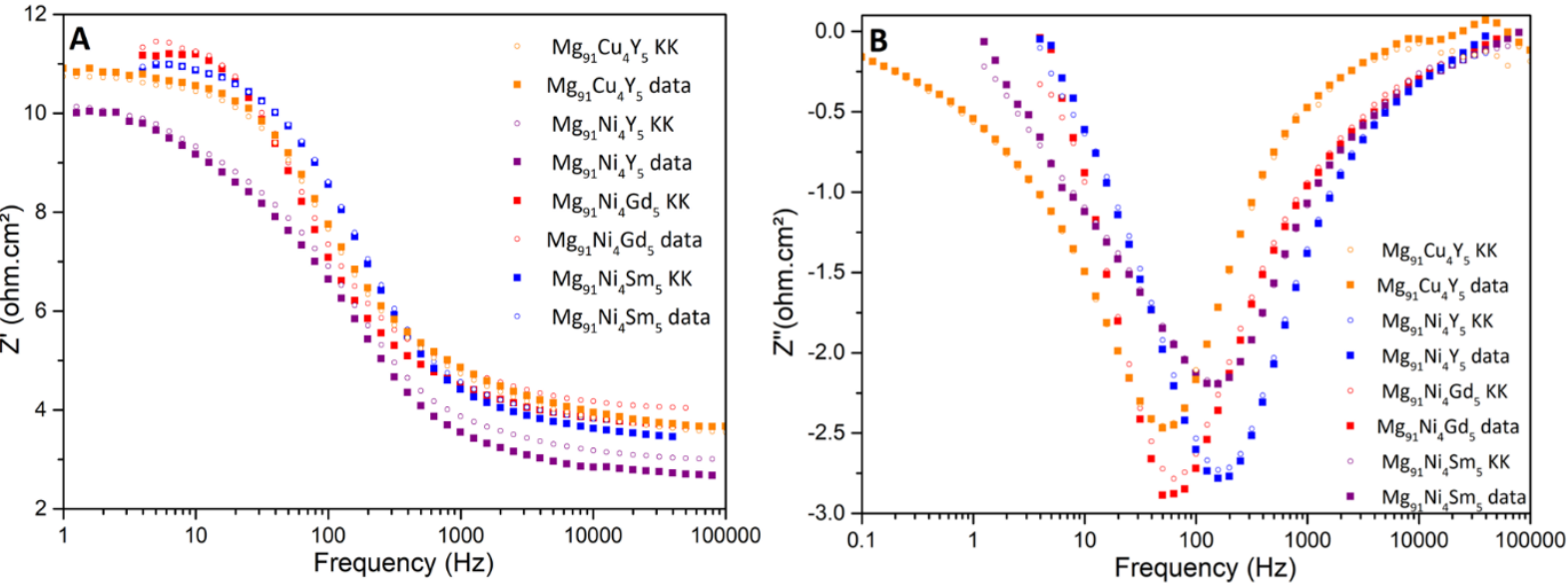


Figure 5: Impedance spectra and Kramers-Kronig (KK) tests for A- Real and B- Imaginary parts.

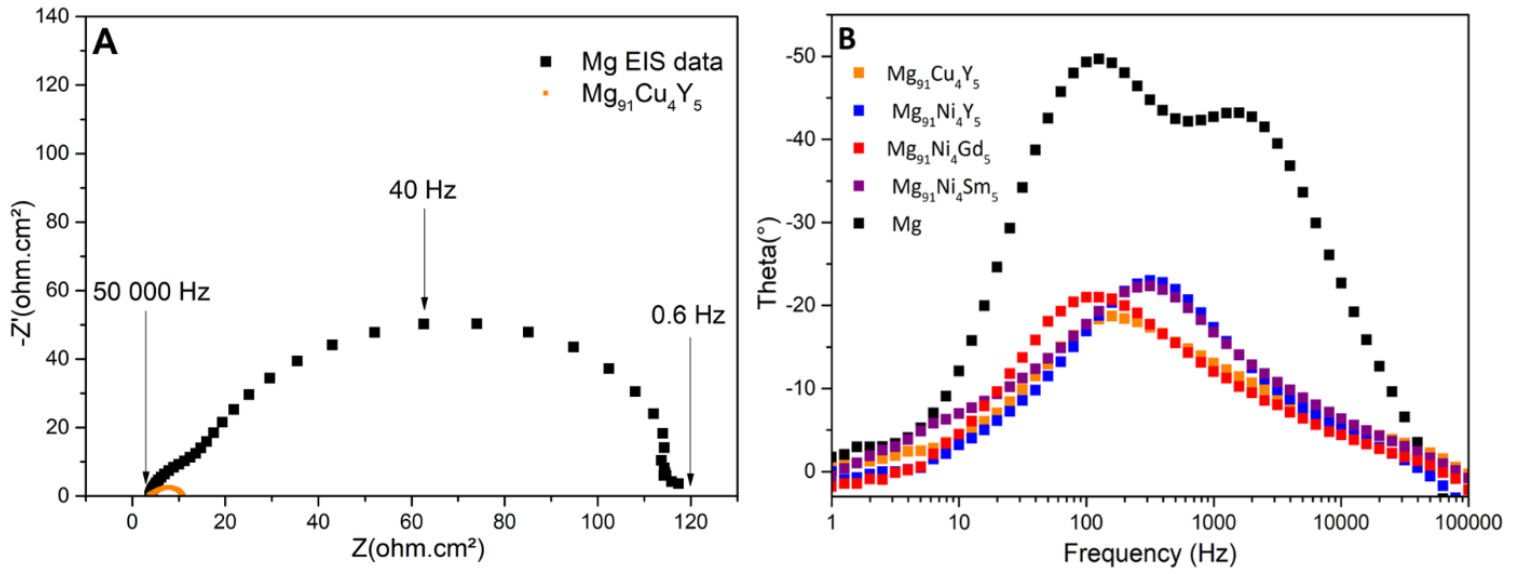


Figure 6 : A- Nyquist plot of Mg and $\text{Mg}_{91}\text{Cu}_4\text{Y}_5$ and B- Phase bode plots for Mg and LPSO alloys.

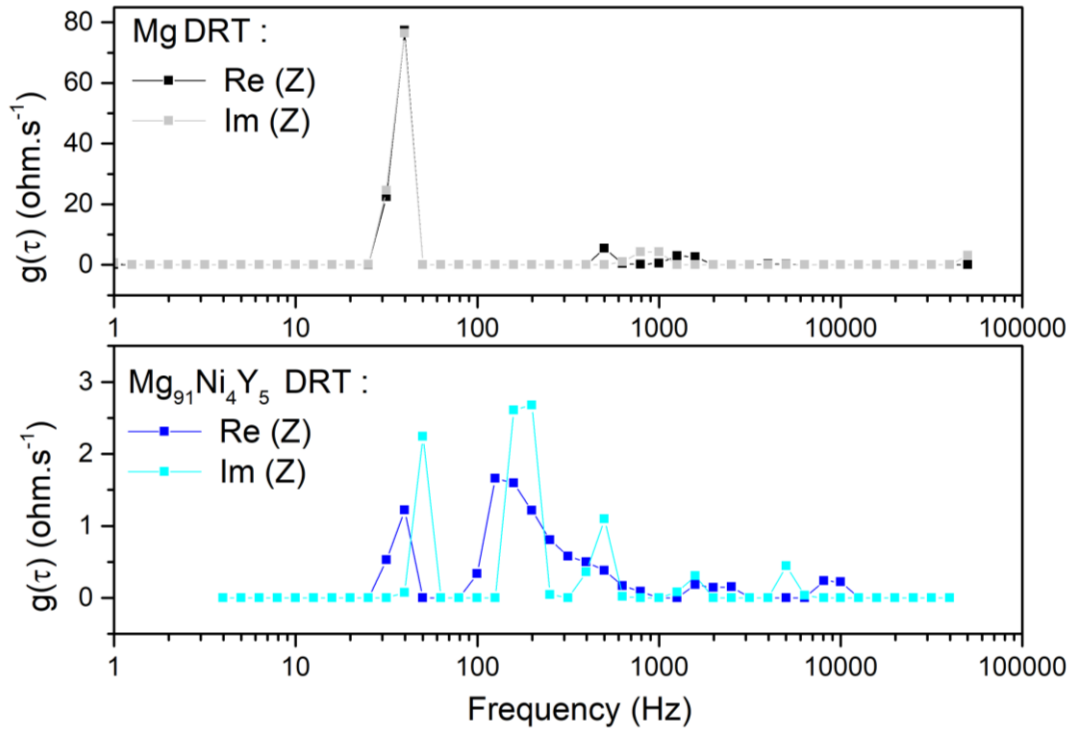


Figure 7 : DRT plots of Mg (top) and $\text{Mg}_{91}\text{Ni}_4\text{Y}_5$ (bottom) calculated with Tikhonov regularization method ($\lambda=10^{-2}$).

Figure 8 shows the equivalent circuit used as well as Nyquist plot of $Mg_{91}Ni_4Gd_5$ and HF and MF contributions simulated independently. According to the preliminary analysis of Mg impedance diagram and the literature on magnesium corrosion [11,21,64], an equivalent circuit with two parallel CPE was used to model EIS data. Initially designed for the corrosion of a metal covered with organic coating, the chosen model appeared to be relevant and widely used for corrosion of bare metals [21,64–66]. The serial resistance R_s is associated to the electrolyte resistance and is measured when frequency tends toward infinite. The double-layer capacitance C_{dl} accounts for charge separation at the electrolyte-material interface. This capacitive behavior shortcuts other phenomena at HF. In order to avoid over-fitting, the different possible interfaces (oxide/electrolyte, hydroxide/electrolyte ...) were not distinguished; their overall contribution is described by a unique CPE. Since the porous oxide/hydroxide film is not perfectly insulating the surface, a film resistance R_f accounts for the current passing through this layer. The adsorption capacitance C_{ads} is the pseudo-capacitive phenomena linked to adsorption of species on the metal surface and occurs in the MF range. The charge transfer resistance R_{ct} at the metal/electrolyte interface is associated in parallel to C_{ads} .

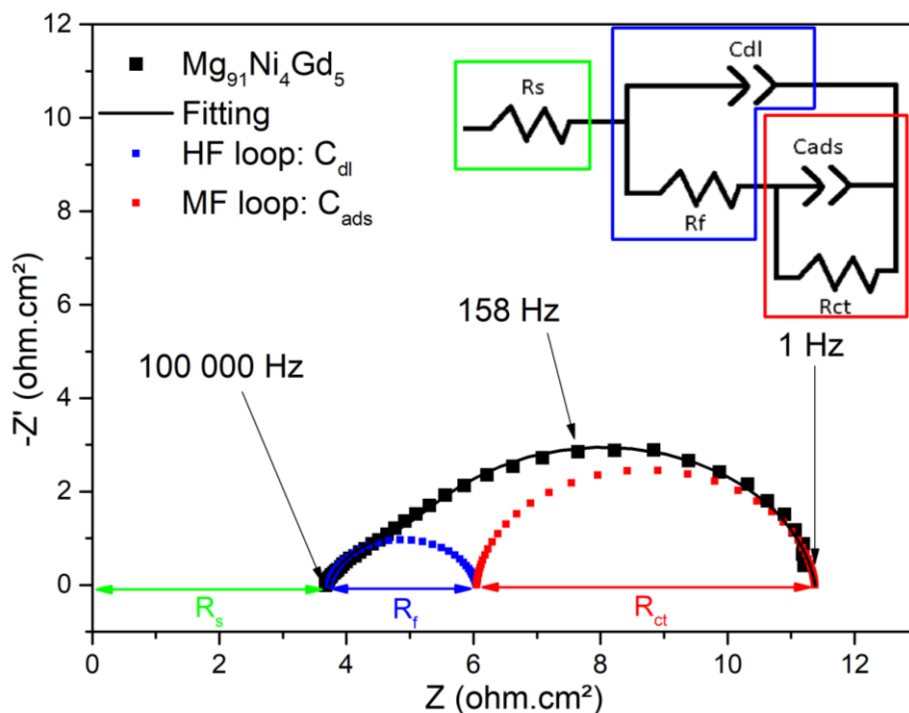


Figure 8 : Nyquist plot of $Mg_{91}Ni_4Gd_5$ and equivalent circuit used for fitting EIS data.

The fitted parameters obtained for all alloys and pure Mg using the equivalent circuit of figure 6 are reported in Table 2. Typical oxide layer capacity is in the order of few tens of $\mu F/cm^2$ [67–70], such values are in good agreement with the C_{dl} measured in the present study (Table 2). The particularly high value of $172 \mu F/cm^2$ obtained for $Mg_{91}Ni_4Sm_5$ indicates that the effective reacting surface of this material has significantly increased during the initial immersion time of 2400s, which is most likely due to crevices and porous hydroxide layer formation. In contrast, the low double layer

capacity C_{dl} of pure Mg ($11 \mu\text{F}/\text{cm}^2$) corresponds to an oxide coating capacity [67,68], meaning that less corrosion occurred on this material surface during the immersion. Indeed, after this immersion period all LPSO are mostly covered of black corrosion products while pure Mg still shows silvery parts which is the color of air formed MgO. This oxide layer covering pure Mg material also explains its higher value of R_f compared to those of LPSO that are covered by $\text{Mg}(\text{OH})_2$ porous layer. The total resistance measured by EIS for LPSO compounds are all very close ($R_s + R_f + R_{ct} \approx 11 \text{ ohm}\cdot\text{cm}^2$) which makes comparisons thorny. However, it can be noticed that $\text{Mg}_{91}\text{Ni}_4\text{Sm}_5$ is the only alloy with such low R_{ct} and high C_{ads} (Table 2), which indicates a strong interaction affinity between metallic surface and ions from the solution.

Table 2 : Fitting results (with approximately 5% accuracy) for EIS measurement performed in 0.6 mol/L NaCl after 2400 s immersion.

Alloy	R_s (ohm.cm ²)	C_{dl} ($\mu\text{F}/\text{cm}^2$)	R_f (ohm.cm ²)	C_{ads} ($\mu\text{F}/\text{cm}^2$)	R_{ct} (ohm.cm ²)
$\text{Mg}_{91}\text{Cu}_4\text{Y}_5$	3.7	52	2.6	210	4.7
$\text{Mg}_{91}\text{Ni}_4\text{Y}_5$	3.4	30	0.9	89	6.8
$\text{Mg}_{91}\text{Ni}_4\text{Gd}_5$	3.7	82	2.3	309	5.3
$\text{Mg}_{91}\text{Ni}_4\text{Sm}_5$	2.7	172	6.8	22545	0.7
Pure Mg	4.2	11	22	35	91

3.2.3. Potentiodynamic polarization

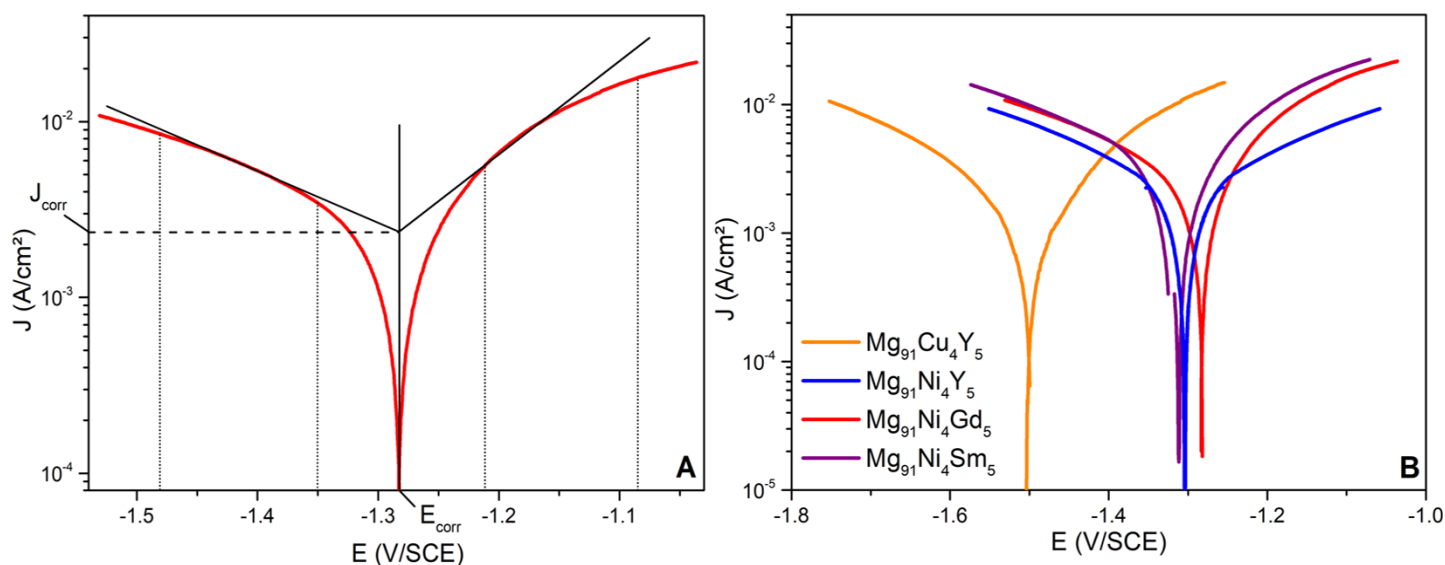


Figure 9 : A- Tafel extrapolation method ($\text{Mg}_{91}\text{Ni}_4\text{Gd}_5$) and B- Polarization curves at 25°C in 0.6 mol/L NaCl solution.

As corrosion is a faradaic process, there is a direct link between the quantity $n(H_2)$ (mol/cm²) of H₂ produced and the corrosion rate of the alloy :

$$n(H_2) = \frac{J_{corr} * t}{F * z} \quad (3)$$

with J_{corr} the corrosion current (A/cm²), t the time (s), F the Faraday constant (96485 C/mol) and z the valance of the species (2). Determining J_{corr} for a material is thus a direct characterization of its ability to produce hydrogen by hydrolysis.

Linear sweep voltametry experiment allowed the construction of Tafel plots ($\log|J| = f(E)$) shown on figure 9. Tafel extrapolation method (figure 9A) was used to determine the corrosion currents densities J_{corr} listed in table 3. Current measured under anodic polarization is characteristic of the dissolution kinetic of the metal (*i.e.* M oxidizes into $M^{n+} + ne^-$). In the case of Mg, interpretation of this measurement is not that trivial because of the anomalous Hydrogen Evolution (HE) observed on anodically polarized surfaces (also known as Negative Difference Effect) [6,14,15,25]. Even though not predicted by conventional corrosion theory, Mg undergoes an increasing HE with increasing potential toward positive values. For this reason, anodic current is underestimated since part of electrons recombine to form H₂ and do not flow in external circuit. Even after IR drop correction, the alloys tend to exhibit higher current densities under anodic polarization than under cathodic. This may be partly due to a non neglectable part of the surface being covered by H₂ bubbles during cathodic polarization. Anomalous HE and partial surface coverage by H₂ bubbles may explain the discrepancies reported for corrosion current values measured by electrochemical means and mass loss and hydrogen collection methods. [6,26]. Despite these points, corrosion current densities reported in Table 3 are in good agreement with hydrolysis experiments since alloys with higher corrosion currents also have higher hydrolysis kinetics. Indeed, while all above-mentioned bias may lead to underestimation of the corrosion current density values determined by Tafel method, the comparisons between alloys is possible since they all undergo these phenomena.

Table 3 : Values obtained from OCP and polarization measurements at 25°C in 0.6 mol/L NaCl solution, average on at least 3 measures and standard deviation in brackets.

Alloy	OCP (V/SCE)	E_{corr} (V/SCE)	J_{corr} (mA/cm ²)
Mg ₉₁ Cu ₄ Y ₅	-1.51 (0.05)	-1.50 (0.01)	1.5 (0.1)
Mg ₉₁ Ni ₄ Y ₅	-1.34 (0.03)	-1.31 (0.01)	2.0 (0.1)
Mg ₉₁ Ni ₄ Gd ₅	-1.33 (0.02)	-1.27 (0.01)	2.2 (0.01)
Mg ₉₁ Ni ₄ Sm ₅	-1.32 (0.01)	-1.32 (0.01)	2.7 (0.1)
Mg	-1.7 (0.02)	-1.65 [71]	0.6 [71]

Corrosion current density of pure Mg by this method has already been reported in the same conditions [71] and is three times inferior to Mg₉₁Cu₄Y₅, the LPSO with lowest corrosion rate (table 3).

The different corrosion rates (and hydrolysis kinetics) observed between the three $Mg_{91}Ni_4RE_5$ alloys may be explained by materials characterizations. It has indeed been demonstrated that phase repartition has a major role on corrosion rates [71], the galvanic corrosion being favored in alloys with more intricate phases. $Mg_{91}Ni_4Y_5$ has a microstructure with larger Mg phases domains (figure 2B) compared to $Mg_{91}Ni_4Gd_5$ and $Mg_{91}Ni_4Sm_5$ (figures 2C and 2D), its corrosion rate and hydrolysis kinetic are also smaller. Even though visible on figures 2C and 2D, microstructural differences between $Mg_{91}Ni_4Gd_5$ and $Mg_{91}Ni_4Sm_5$ are more difficult to analyze. The actual chemical composition of the LPSO may explain the slight corrosion kinetics between these two alloys. EDXS analyses of LPSO given in table 1 show that Sm-14H (LPSO in $Mg_{91}Ni_4Sm_5$) contains a higher Ni proportion compared to Gd-14H (LPSO in $Mg_{91}Ni_4Gd_5$). This LPSO nobility difference may lead to both stronger micro galvanic coupling with Mg and higher inner LPSO corrosion (stronger coupling between Mg and Mg-RE-TM layers within the LPSO).

3.2.4. Electrochemical measurements using Rotating Disk Electrode (RDE)

Using Rotating Disc Electrode (RDE) allows controlling the convection effect in the electrolyte and leads to electrochemical measurements on a rotating surface that helps the diffusion of species in the electrolyte near the reacting surface. If the corrosion mechanism is limited by mass transport, the inverse of the measured current should evolve as the inverse of the squared root of the electrode rotation speed [72,73]. However, according to Tafel plots reported on figure 10 for $Mg_{91}Ni_4Y_5$ at 25°C in 0.6 mol/L NaCl solution it seems that the rotation speed has no effect on the polarization curves

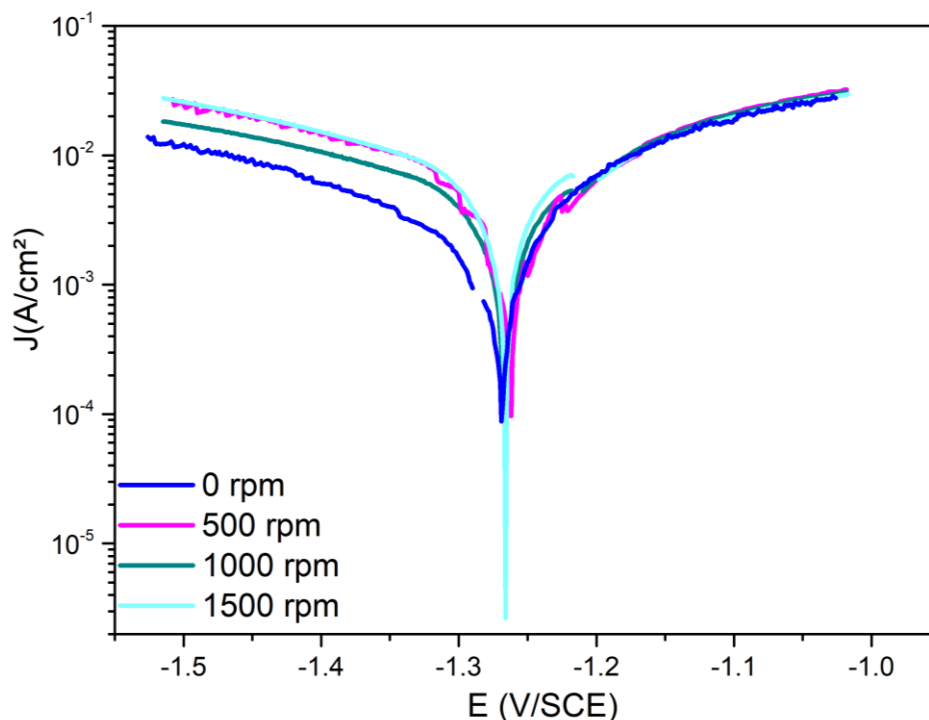


Figure 10 : Polarization curves of $Mg_{91}Ni_4Y_5$ at 25°C in 0.6 mol/L NaCl solution for different rotation speeds.

recorded on $Mg_{91}Ni_4Y_5$ electrode material. Indeed, anodic polarization domain ($E > -1.2V/ECS$) of all rotation speed (0 to 1500 rpm) superimposes. On the cathodic side, the differences of current density values are assigned to hydrogen bubbles covering (randomly) the surface from electrolyte. This is also the reason why these measurements are noisy. The same experiment has been done on $Mg_{91}Ni_4Gd_5$ with rotation speed in the range 2000 to 5000 rpm and similar results were obtained. Electrochemical characterization using RDE confirms that mass transport (*i.e.* diffusion) is not the limiting step in the corrosion process of LPSO and cannot explain the difference in corrosion current densities between the compounds.

3.2.5. Effect of immersion time

Figure 11A shows the OCP evolution for $Mg_{91}Cu_4Y_5$ with corrosion currents estimated by Tafel method at different immersion times. The associated current density recorded at $t=500$; 2400 and 4000s have been reported on the figure 11A. In addition, EIS diagrams have also been measured at the same selected immersion times (see figure 11B). It can be noticed that the corrosion current density values tend to increase with immersion time for two reasons :

- (i) The longer the sample is immersed the less passivated regions remain and the more regions start to corrode (surface is “activated”).
- (ii) During the OCP immersion where corrosion propagates, the actual surface of the sample increases with forming pits and crevices. The surface by which recorded current is normalised is the geometrical surface measured prior to the test and is necessarily smaller than the real surface.

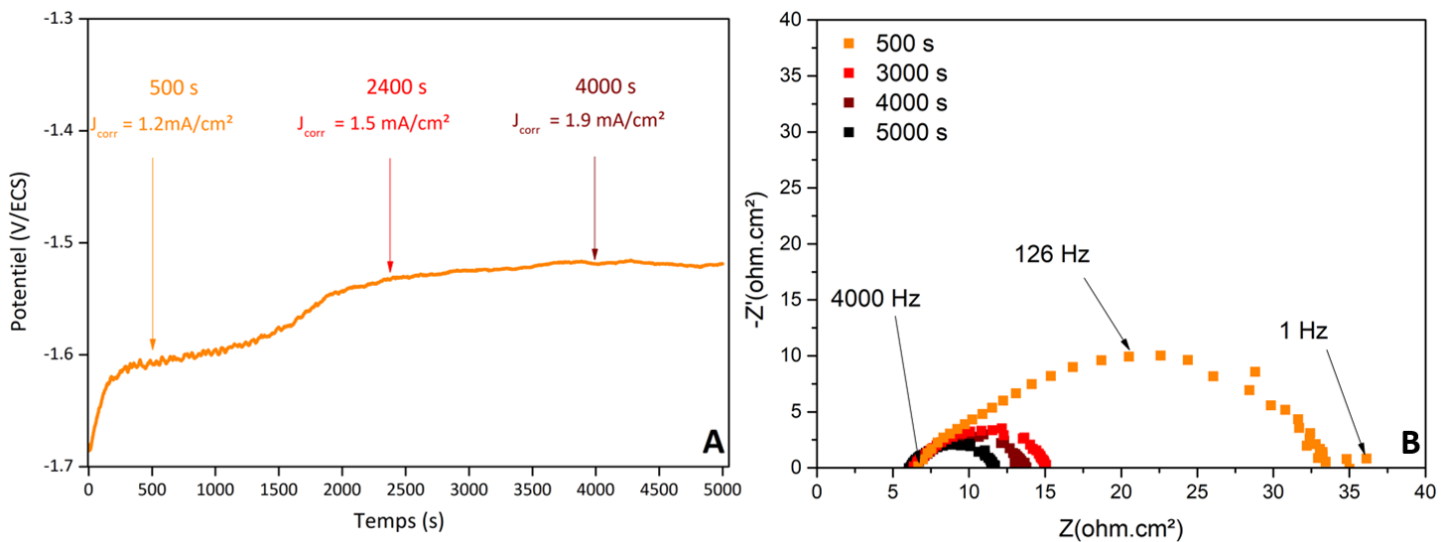


Figure 11 : Effect of immersion time in 0.6 mol/L NaCl solution on $Mg_{91}Cu_4Y_5$: A- OCP and corrosion currents and B- Nyquist plot of EIS data.

Table 4 : Fitting results (with approximately 5% accuracy) for EIS measurement performed in 0.6 mol/L NaCl at different immersion times for $Mg_{91}Cu_4Y_5$.

Immersion time (s)	R_s (ohm.cm ²)	C_{dl} (μF/cm ²)	R_f (ohm.cm ²)	C_{ads} (μF/cm ²)	R_{ct} (ohm.cm ²)
500	7.1	19	7.1	59	19
3000	6.6	110	3.0	230	5.5
4000	6.6	145	2.7	17	4.3
5000	6.3	181	2.4	24	3.0

EIS diagrams measured for $Mg_{91}Cu_4Y_5$ at different immersion times show similar shapes but have significantly different amplitudes. Figure 11B shows that the overall resistance of the system is smaller when the immersion time increases. This is consistent with the polarization experiment where an increase of the current with immersion time is observed. EIS data has been fitted using the equivalent circuit exposed earlier and results are shown in Table 4. R_f and R_{ct} values decrease with immersion time and can be associated to MgO passive layer replacement by porous Mg(OH)₂. After about 1700s, the OCP also shifts abruptly towards higher values, which can only be explained by a significant diminution of Mg proportion on the surface. Double layer capacitance C_{dl} values are increasing linearly with immersion time, which confirms the statement made in EIS section that C_{dl} reflects the physical evolution of the surface (active surface area). This point is further supported by SEM micrographs of figure 12 that show the important surface modification associated with immersion time.

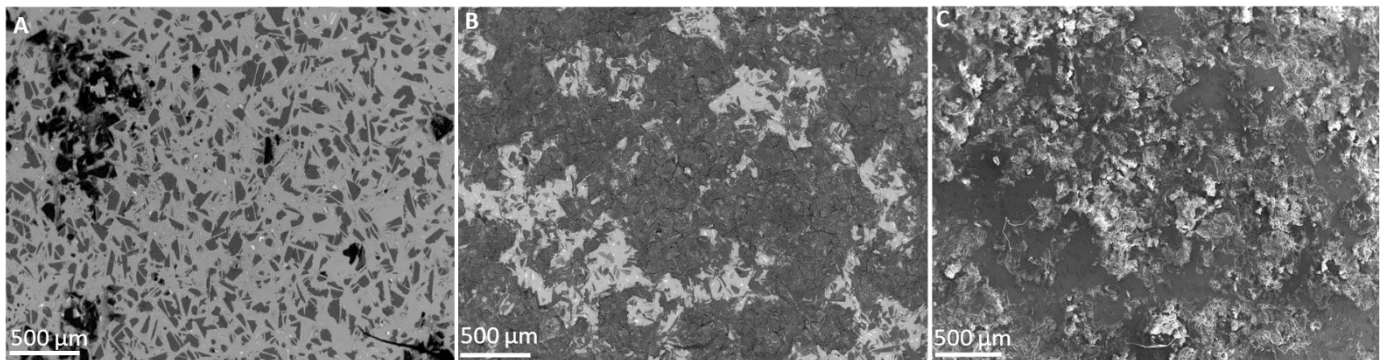


Figure 12 : Evolution of $Mg_{91}Cu_4Y_5$ surface with immersion time : A- 500s (BSE), B-5000s (BSE) and C-5000s (SE).

Electrochemical measurements analytically enlightened the different hydrolysis properties observed on powders. Potentiodynamic polarization (*i.e.* J_{corr} determination) emphasized the kinetic differences recorded between the alloys during hydrolysis experiment. OCP measurement showed that thermodynamic stability of the systems is more dependent on the presence of transition metal than that of rare earth. The electrochemical impedance spectroscopy did not show major corrosion mechanism differences between Mg and LPSO (*i.e.* same shape of Nyquist diagram) but an important difference of impedance magnitude, which showed the very small corrosion resistance of LPSO alloys.

When analyzing corrosion on bulk material, corrosion rates increase and impedance diminish because the reacting surface increases. However, in hydrolysis experiment on powders, the kinetic is maximal in the initial stage and decreases as available reactant is consumed. Despite these different testing conditions, the results obtained with electrochemical tests are coherent with hydrolysis experiment.

4. Conclusion

Four alloys with high 14H-LPSO content ($Mg_{91}Cu_4Y_5$; $Mg_{91}Ni_4Y_5$; $Mg_{91}Ni_4Gd_5$; $Mg_{91}Ni_4Sm_5$) were synthesized from different elements (Mg + Ni or Cu + Y, Gd or Sm) in order to compare their electrochemical properties with their hydrogen generation performances as powders. The main results of this study are summarized as follows:

- Good correlation was observed between hydrolysis experiments and electrochemical measurements, highlighting the relevance of surface characterization on bulk materials for understanding hydrogen generation by hydrolysis with powder.
- 14H LPSO structures have high corrosion current densities and low impedance values compared to pure Mg, reflecting their strong ability to corrode in seawater. These results explain the good hydrogen generation kinetics obtained from powders of these materials.
- Changing the nature of the rare earth (Y, Gd or Sm) and of the transition element (Ni or Cu) in the alloy resulted in both microstructural and LPSO chemical composition differences.
- These differences in turn influenced the corrosion rates determined by Tafel method as the alloys with most intricate Mg-LPSO phases and LPSO with higher Ni content happened to corrode faster.
- The double layer capacity C_{dl} , measured by impedance spectroscopy after a given immersion time informed, in an indirect manner, on the alloy ability to corrode by informing on the actively reacting surface.
- 14H-LPSO corrosion rate is not controlled by diffusion processes.

Depicting further the fundamental corrosion mechanisms would be greatly helped with lower scale characterization of LPSO.

Declaration of competing interest

The authors declare that they have no known competing financial interests or personal relationships that could have appeared to influence the work reported in this paper.

Acknowledgment

This work was financially supported by Direction Générale de l'Armement and Région Nouvelle Aquitaine through a grant to Manuel Legrée.

Bibliography

- [1] Fleischer M. Recent estimates of the abundances of the elements in this earth's crust. vol. 285. 1953. <https://doi.org/https://doi.org/10.3133/cir285>.
- [2] Mordike BL, Ebert T. Magnesium Properties - applications - potential. Mater Sci Eng A 2001;302:37–45. [https://doi.org/10.1016/S0921-5093\(00\)01351-4](https://doi.org/10.1016/S0921-5093(00)01351-4).
- [3] Monteiro WA. The Influence of Alloy Element on Magnesium for Electronic Devices Applications – A Review. Light Met Alloy Appl 2014;229–41. <https://doi.org/10.5772/58460>.
- [4] Kamado S. Magnesium alloys and their application. vol. 60. 2010. <https://doi.org/10.2464/jilm.60.100>.
- [5] Wang J, Gao S, Liu X, Peng X, Wang K, Liu S, et al. Enhanced mechanical properties and degradation rate of Mg–Ni–Y alloy by introducing LPSO phase for degradable fracturing ball applications. J Magnes Alloy 2020;8:127–33. <https://doi.org/10.1016/j.jma.2019.11.010>.
- [6] Esmaily M, Svensson JE, Fajardo S, Birbilis N, Frankel GS, Virtanen S, et al. Fundamentals and advances in magnesium alloy corrosion. Prog Mater Sci 2017;89:92–193. <https://doi.org/10.1016/j.pmatsci.2017.04.011>.
- [7] Zong X, Zhang J, Liu W, Zhang Y, You Z, Xu C. Corrosion Behaviors of Long-Period Stacking Ordered Structure in Mg Alloys Used in Biomaterials: A Review. Adv Eng Mater 2018;20:1–26. <https://doi.org/10.1002/adem.201800017>.
- [8] Samaniego A, Hurley BL, Frankel GS. On the evidence for univalent Mg. J Electroanal Chem 2015;737:123–8. <https://doi.org/10.1016/j.jelechem.2014.04.013>.
- [9] Guang B, Song L, Atrens A. Corrosion Mechanisms of Magnesium Alloys ** 2000:11–33.
- [10] Birbilis N, Easton MA, Sudholz AD, Zhu SM, Gibson MA. On the corrosion of binary magnesium-rare earth alloys. Corros Sci 2009;51:683–9. <https://doi.org/10.1016/j.corsci.2008.12.012>.

- [11] Bland LG, Gusieva K, Scully JR. Effect of Crystallographic Orientation on the Corrosion of Magnesium: Comparison of Film Forming and Bare Crystal Facets using Electrochemical Impedance and Raman Spectroscopy. *Electrochim Acta* 2017;227:136–51. <https://doi.org/10.1016/j.electacta.2016.12.107>.
- [12] Gusieva K, Davies CHJ, Scully JR, Birbilis N. Corrosion of magnesium alloys: The role of alloying. *Int Mater Rev* 2015;60:169–94. <https://doi.org/10.1179/1743280414Y.0000000046>.
- [13] Banjade DR. Fundamental Investigation of Magnesium Corrosion Using Experiments and Simulation 2018:135.
- [14] Atrens A, Song GL, Cao F, Shi Z, Bowen PK. Advances in Mg corrosion and research suggestions. *J Magnes Alloy* 2013;1:177–200. <https://doi.org/10.1016/j.jma.2013.09.003>.
- [15] Li Y, Shi Z, Chen X, Atrens A. Anodic hydrogen evolution on Mg. *J Magnes Alloy* 2021;9:2049–62. <https://doi.org/10.1016/j.jma.2021.09.002>.
- [16] Frankel GS, Samaniego A, Birbilis N. Evolution of hydrogen at dissolving magnesium surfaces. *Corros Sci* 2013;70:104–11. <https://doi.org/10.1016/j.corsci.2013.01.017>.
- [17] Fajardo S, Frankel GS. Effect of impurities on the enhanced catalytic activity for hydrogen evolution in high purity magnesium. *Electrochim Acta* 2015;165:255–67. <https://doi.org/10.1016/j.electacta.2015.03.021>.
- [18] Huang J, Song G, Zhu Y, Zheng D, Wang Z. The anodically polarized Mg surface products and accelerated hydrogen evolution. *J Magnes Alloy* 2021. <https://doi.org/10.1016/j.jma.2021.05.008>.
- [19] Delgado MC, García-Galvan FR, Barranco V, Batlle SF. A Measuring Approach to Assess the Corrosion Rate of Magnesium Alloys Using Electrochemical Impedance Spectroscopy. *Magnes Alloy* 2017. <https://doi.org/10.5772/65018>.
- [20] Samaniego A, Birbilis N, Xia X, Frankel GS. Hydrogen evolution during anodic polarization of Mg alloyed with Li, Ca, or Fe. *Corrosion* 2015;71:224–33. <https://doi.org/10.5006/1367>.
- [21] King AD, Birbilis N, Scully JR. Accurate Electrochemical Measurement of Magnesium Corrosion Rates; a Combined Impedance , Mass-Loss and Hydrogen Collection Study. *Electrochim Acta* 2014;121:394–406. <https://doi.org/10.1016/j.electacta.2013.12.124>.
- [22] Leleu S, Rives B, Causse N, Pébère N. Corrosion rate determination of rare-earth Mg alloys in a Na₂SO₄ solution by electrochemical measurements and inductive coupled plasma-optical

- emission spectroscopy. *J Magnes Alloy* 2019;7:47–57. <https://doi.org/10.1016/j.jma.2018.12.002>.
- [23] Al Asmar E, Tencé S, Bobet JL, Ourane B, Nakhl M, Zakhour M, et al. The Mg-Rich Phase NdNiMg15: Structural and Magnetic Properties. *Inorg Chem* 2018;57:14152–8. <https://doi.org/10.1021/acs.inorgchem.8b02007>.
- [24] Thomas S, Medhekar N V., Frankel GS, Birbilis N. Corrosion mechanism and hydrogen evolution on Mg. *Curr Opin Solid State Mater Sci* 2015;19:85–94. <https://doi.org/10.1016/j.cossms.2014.09.005>.
- [25] Esmaily M, Svensson JE, Fajardo S, Birbilis N, Frankel GS, Virtanen S, et al. Anomalous hydrogen evolution on AZ31, AZ61 and AZ91 magnesium alloys in unbuffered sodium chloride solution. *Prog Mater Sci* 2017;146:92–193. <https://doi.org/10.1016/j.pmatsci.2017.04.011>.
- [26] Pardo A, Feliu S, Merino MC, Arrabal R, Matykina E. Electrochemical estimation of the corrosion rate of magnesium/aluminium alloys. *Int J Corros* 2010;2010:7–13. <https://doi.org/10.1155/2010/953850>.
- [27] Uesugi H, Sugiyama T, Nakatsugawa I, Ito T. Production of hydrogen storage material MgH₂ and its application. *Keikinzoku/Journal Japan Inst Light Met* 2010;60:615–8. <https://doi.org/10.2464/jilm.60.615>.
- [28] Kantürk Figen A, Coşkuner B, Pişkin S. Hydrogen generation from waste Mg based material in various saline solutions (NiCl₂, CoCl₂, CuCl₂, FeCl₃, MnCl₂). *Int J Hydrogen Energy* 2015;40:7483–9. <https://doi.org/10.1016/j.ijhydene.2015.01.022>.
- [29] Grosjean MH, Zidoune M, Roué L. Hydrogen production from highly corroding Mg-based materials elaborated by ball milling. *J Alloys Compd* 2005;404–406:712–5. <https://doi.org/10.1016/j.jallcom.2004.10.098>.
- [30] Sabatier J, Mauvy F, Bobet J-L, Mohedano D, Faessel M, Bos F. A New Device for Hydrogen Production on Demand with Application to Electric Assist Bike: Description, Production Characteristics and Basic Control. n.d.
- [31] Oh SK, Cho TH, Kim MJ, Lim JH, Eom KS, Kim DH, et al. Fabrication of Mg–Ni–Sn alloys for fast hydrogen generation in seawater. *Int J Hydrogen Energy* 2017;42:7761–9. <https://doi.org/10.1016/j.ijhydene.2016.11.138>.
- [32] Al Bacha S, Awad AS, El Asmar E, Tayeh T, Bobet JL, Nakhl M, et al. Hydrogen generation via hydrolysis of ball milled WE43 magnesium waste. *Int J Hydrogen Energy* 2019;44:17515–24.

<https://doi.org/10.1016/j.ijhydene.2019.05.123>.

- [33] Hou X, Shi H, Yang L, Feng L, Suo G, Ye X, et al. Comparative investigation on feasible hydrolysis H₂ production behavior of commercial Mg-M (M = Ni, Ce, and La) binary alloys modified by high-energy ball milling—Feasible modification strategy for Mg-based hydrogen producing alloys. *Int J Energy Res* 2020;1–17. <https://doi.org/10.1002/er.5843>.
- [34] Saal JE, Wolverton C. Thermodynamic stability of Mg-based ternary long-period stacking ordered structures. *Acta Mater* 2014;68:325–38. <https://doi.org/10.1016/j.actamat.2013.10.055>.
- [35] Kishida K, Nagai K, Matsumoto A, Yasuhara A, Inui H. Crystal structures of highly-ordered long-period stacking-ordered phases with 18R, 14H and 10H-type stacking sequences in the Mg-Zn-Y system. *Acta Mater* 2015;99:228–39. <https://doi.org/10.1016/j.actamat.2015.08.004>.
- [36] Mi SB, Jin QQ. New polytypes of long-period stacking ordered structures in Mg-Co-Y alloys. *Scr Mater* 2013;68:635–8. <https://doi.org/10.1016/j.scriptamat.2012.12.025>.
- [37] Kim JK, Guo W, Choi PP, Raabe D. Compositional evolution of long-period stacking ordered structures in magnesium studied by atom probe tomography. *Scr Mater* 2018;156:55–9. <https://doi.org/10.1016/j.scriptamat.2018.07.017>.
- [38] Li CQ, Xu DK, Zeng ZR, Wang BJ, Sheng LY, Chen XB, et al. Effect of volume fraction of LPSO phases on corrosion and mechanical properties of Mg-Zn-Y alloys. *Mater Des* 2017;121:430–41. <https://doi.org/10.1016/j.matdes.2017.02.078>.
- [39] Liu J, Yang L, Zhang C, Zhang B, Zhang T, Li Y, et al. Role of the LPSO structure in the improvement of corrosion resistance of Mg-Gd-Zn-Zr alloys. *J Alloys Compd* 2019;782:648–58. <https://doi.org/10.1016/j.jallcom.2018.12.233>.
- [40] Inoue A, Kawamura Y, Matsushita M, Hayashi K, Koike J. Novel hexagonal structure and ultrahigh strength of magnesium solid solution in the Mg-Zn-Y system. *J Mater Res* 2001;16:1894–900. <https://doi.org/10.1557/JMR.2001.0260>.
- [41] Abe E, Kawamura Y, Hayashi K, Inoue A. Long-period ordered structure in a high-strength nanocrystalline Mg-1 at% Zn-2 at% Y alloy studied by atomic-resolution Z-contrast STEM. *Acta Mater* 2002;50:3845–57. [https://doi.org/10.1016/S1359-6454\(02\)00191-X](https://doi.org/10.1016/S1359-6454(02)00191-X).
- [42] Kawamura Y, Yamasaki M. Formation and mechanical properties of Mg₉₇Zn₁RE₂ alloys with long-period stacking ordered structure. *Mater Trans* 2007;48:2986–92. <https://doi.org/10.2320/matertrans.MER2007142>.

- [43] Yamasaki M, Matsushita M, Hagihara K, Izuno H, Abe E, Kawamura Y. Highly ordered 10H-type long-period stacking order phase in a Mg-Zn-Y ternary alloy. *Scr Mater* 2014;78–79:13–6. <https://doi.org/10.1016/j.scriptamat.2014.01.013>.
- [44] Cheng P, Zhao Y, Lu R, Hou H. Effect of the morphology of long-period stacking ordered phase on mechanical properties and corrosion behavior of cast Mg-Zn-Y-Ti alloy. *J Alloys Compd* 2018;764:226–38. <https://doi.org/10.1016/j.jallcom.2018.06.056>.
- [45] Zong X, Zhang J, Liu W, Chen J, Nie K, Xu C. Effects of Li on Microstructures, Mechanical, and Biocorrosion Properties of Biodegradable Mg94-xZn2Y4Lix Alloys with Long Period Stacking Ordered Phase. *Adv Eng Mater* 2017;19:1–8. <https://doi.org/10.1002/adem.201600606>.
- [46] Han Z, Zhang K, Yang J, Wei R, Liu Y, Zhang C. The Anodic Role of Ni-Containing LPSO Phases During the Microgalvanic Corrosion of Mg 98 Gd 1.5 Ni 0.5 Alloy. *J Mater Eng Perform* 2019;28:2451–8. <https://doi.org/10.1007/s11665-019-04018-x>.
- [47] Legrée M, Charbonnier V, Al Bacha S, Asano K, Sakaki K, Aubert I, et al. Hydrogen generation by hydrolysis reaction using magnesium alloys with long period stacking ordered structure. *Int J Hydrogen Energy* 2021;6:2–12. <https://doi.org/10.1016/j.ijhydene.2021.08.087>.
- [48] Al Bacha S, Pighin SA, Urretavizcaya G, Zakhour M, Nakhl M, Castro FJ, et al. Effect of ball milling strategy (milling device for scaling-up) on the hydrolysis performance of Mg alloy waste. *Int J Hydrogen Energy* 2020;45:20883–93. <https://doi.org/10.1016/j.ijhydene.2020.05.214>.
- [49] Tayeh T, Awad AS, Nakhl M, Zakhour M, Silvain JF, Bobet JL. Production of hydrogen from magnesium hydrides hydrolysis. *Int J Hydrogen Energy* 2014;39:3109–17. <https://doi.org/10.1016/j.ijhydene.2013.12.082>.
- [50] Zeimet B, Flura A, Grenier J, Mauvy F, Zeimet B, Flura A, et al. Using the Distribution of Relaxation Times for analyzing the Kramers-Kronig Relations in Electrochemical Impedance Spectroscopy. vol. 1. 2018.
- [51] Pighin SA, Urretavizcaya G, Bobet JL, Castro FJ. Nanostructured Mg for hydrogen production by hydrolysis obtained by MgH₂ milling and dehydriding. *J Alloys Compd* 2020;827. <https://doi.org/10.1016/j.jallcom.2020.154000>.
- [52] Yokobayashi H, Kishida K, Inui H, Yamasaki M, Kawamura Y. Enrichment of Gd and Al atoms in the quadruple close packed planes and their in-plane long-range ordering in the long period stacking-ordered phase in the Mg-Al-Gd system. *Acta Mater* 2011;59:7287–99. <https://doi.org/10.1016/j.actamat.2011.08.011>.

- [53] Kishida K, Yokobayashi H, Inui H, Yamasaki M, Kawamura Y. The crystal structure of the LPSO phase of the 14 H-type in the Mg-Al-Gd alloy system. *Intermetallics* 2012;31:55–64. <https://doi.org/10.1016/j.intermet.2012.06.010>.
- [54] Jiang M, Zhang S, Bi Y, Li H, Ren Y, Qin G. Phase equilibria of the long-period stacking ordered phase in the Mg-Ni-Y system. *Intermetallics* 2015;57:127–32. <https://doi.org/10.1016/j.intermet.2014.10.014>.
- [55] Charbonnier V, Asano K, Kim H, Sakaki K. Hydrogenation Properties of Mg_{83.3} Cu_{7.2} Y_{9.5} with Long Period Stacking Ordered Structure and Formation of Polymorphic γ -MgH₂. *Inorg Chem* 2020;59:0–11. <https://doi.org/10.1021/acs.inorgchem.0c02080>.
- [56] Inoue K, Yoshida K, Nagai Y, Kishida K, Inui H. Correlative atom probe tomography and scanning transmission electron microscopy reveal growth sequence of LPSO phase in Mg alloy containing Al and Gd. *Sci Rep* 2021;11:1–8. <https://doi.org/10.1038/s41598-021-82705-3>.
- [57] Kishida K, Yokobayashi H, Inui H. A formation criterion for Order-Disorder (OD) phases of the Long-Period Stacking Order (LPSO)-type in Mg-Al-RE (Rare Earth) Ternary Systems. *Sci Rep* 2017;7:1–11. <https://doi.org/10.1038/s41598-017-12506-0>.
- [58] Awad AS, El-Asmar E, Tayeh T, Mauvy F, Nakhl M, Zakhour M, et al. Effect of carbons (G and CFs), TM (Ni, Fe and Al) and oxides (Nb₂O₅ and V₂O₅) on hydrogen generation from ball milled Mg-based hydrolysis reaction for fuel cell. *Energy* 2016;95:175–86. <https://doi.org/10.1016/j.energy.2015.12.004>.
- [59] Alasmar E, Awad AS, Hachem D, Tayeh T, Nakhl M, Zakhour M, et al. Hydrogen generation from Nd-Ni-Mg system by hydrolysis reaction. *J Alloys Compd* 2018;740:52–60. <https://doi.org/10.1016/j.jallcom.2017.12.305>.
- [60] Chen XB, Cain T, Scully JR, Birbilis N. Technical note: Experimental survey of corrosion potentials for rare earth metals Ce, Er, Gd, La, and Nd as a function of pH and chloride concentration. *Corrosion* 2014;70:323–8. <https://doi.org/10.5006/1146>.
- [61] del Rosario Silva Campos M. *the Role of Intermetallic Phases in the Corrosion of Magnesium-Rare Earth Alloys*. 2016.
- [62] Dierickx S, Weber A, Ivers-Tiffée E. How the distribution of relaxation times enhances complex equivalent circuit models for fuel cells. *Electrochim Acta* 2020;355:136764. <https://doi.org/10.1016/j.electacta.2020.136764>.
- [63] Ivers-tiffée E, Weber A. Evaluation of electrochemical impedance spectra by the distribution of

relaxation times 2017:193–201.

- [64] Curioni M, Scenini F, Monetta T, Bellucci F. Correlation between electrochemical impedance measurements and corrosion rate of magnesium investigated by real-time hydrogen measurement and optical imaging. *Electrochim Acta* 2015;166:372–84. <https://doi.org/10.1016/j.electacta.2015.03.050>.
- [65] Córdoba-torres P, Mesquita TJ, Devos O, Tribollet B, Roche V, Nogueira RP. On the intrinsic coupling between constant-phase element parameters alpha and Q in electrochemical impedance spectroscopy. *Electrochim Acta* 2012;72:172–8. <https://doi.org/10.1016/j.electacta.2012.04.020>.
- [66] Ivanova N, Gugleva V, Dobрева M, Pehlivanov I, Stefanov S, Andonova V. Electrochemical Impedance Spectroscopy (EIS): A Review Study of Basic Aspects of the Corrosion Mechanism Applied to Steels. *Intech* 2016;i:13. <https://doi.org/10.5772/intechopen.94470>.
- [67] Baril G, Galicia G, Deslouis C, Pébère N, Tribollet B, Vivier V. An Impedance Investigation of the Mechanism of Pure Magnesium Corrosion in Sodium Sulfate Solutions. *J Electrochem Soc* 2007;154:C108. <https://doi.org/10.1149/1.2401056>.
- [68] Jorcin JB, Orazem ME, Pébère N, Tribollet B. CPE analysis by local electrochemical impedance spectroscopy. *Electrochim Acta* 2006;51:1473–9. <https://doi.org/10.1016/j.electacta.2005.02.128>.
- [69] Fontana MG. *Corrosion Engineering*. Third edit. 1985.
- [70] Perez N. *ELECTROCHEMISTRY AND CORROSION SCIENCE*. Kluwer Academic; 2004.
- [71] Alasmar E, Aubert I, Durand A, Nakhl M, Zakhour M, Gaudin E, et al. Hydrogen generation from Mg–NdNiMg 15 composites by hydrolysis reaction. *Int J Hydrogen Energy* 2019;44:523–30. <https://doi.org/10.1016/j.ijhydene.2018.10.233>.
- [72] Amira S, Ferkhi M, Belghobsi M, Khaled A, Mauvy F, Grenier JC. Synthesis, characterization, and electrochemical behavior of a new Nd_{1.9}Sr_{0.1}Ni_{0.9}Co_{0.1}O_{4 ± Δ} material as electrocatalyst for the oxygen reduction reaction. *Ionics (Kiel)* 2019;25:3799–807. <https://doi.org/10.1007/s11581-019-02922-9>.
- [73] Amira S, Ferkhi M, Khaled A, Mauvy F, Grenier JC, Houssiau L, et al. Carbon-based lanthanum nickelate material La_{2-x-y}Nd_xPryNiO_{4+Δ} (x = 0, 0.3, and 0.5; y = 0 and 0.2) as a bifunctional electrocatalyst for oxygen reduction in alkaline media. *Ionics (Kiel)* 2019;25:3809–22. <https://doi.org/10.1007/s11581-019-02963-0>.

